Discovery of ST2 centers in natural and CVD diamond

Jonas Foglszinger, Andrej Denisenko, Georgy V. Astakhov, Lev Kazak, Petr Siyushev, Alexander M. Zaitsev, Jens Fuhrmann, Matthias Schreck, Fedor Jelezko, Roman Kolesov, Jörg Wrachtrup

Angaben zur Veröffentlichung / Publication details:

Foglszinger, Jonas, Andrej Denisenko, Georgy V. Astakhov, Lev Kazak, Petr Siyushev, Alexander M. Zaitsev, Jens Fuhrmann, et al. 2026. "Discovery of ST2 centers in natural and CVD diamond." *npj Quantum Information* 12 (1): 42. https://doi.org/10.1038/s41534-025-01116-8.

npj | quantum information

Article

Published in partnership with The University of New South Wales

https://doi.org/10.1038/s41534-025-01116-8

Discovery of ST2 centers in natural and CVD diamond

Jonas Foglszinger[1] ✉, Andrej Denisenko[1], Georgy V. Astakhov[2], Lev Kazak[3], Petr Siyushev[4], Alexander M. Zaitsev[5], Jens Fuhrmann[3], Matthias Schreck[6], Fedor Jelezko[3,7], Roman Kolesov[1] & Jörg Wrachtrup[1,8]

The ST2 center is an optically addressable point defect in diamond that facilitates spin initialization and readout at room temperature. However, while this study presents the discovery of photostable ST2 centers first observed in a natural diamond and provides a reliable technique for artificially creating them, its chemical structure remains unknown. To assess the potential of ST2, we map out its basic optical characteristics, reveal its electronic level structure, and quantify the intrinsic transition rates. Furthermore, we investigate its response to microwaves, static magnetic fields, and the polarization of excitation laser light, revealing twelve inequivalent orientations of the ST2 center. Simultaneous exposure to microwaves and static magnetic fields also reveals an exceptionally wide acceptance angle for sensing strong magnetic fields, unlike the well-established NV center, which is sensitive only within a narrow cone aligned with its symmetry axis. This finding establishes the ST2 center as a highly promising candidate for nanoscale quantum sensing.

Exploring the intricacies of condensed matter physics at the smallest scales has driven the pursuit of nanoscale sensors[1–3]. Spatial resolution is inherently dependent on the physical dimensions of the sensor unit. This makes sensors based on single defects exhibiting optically detected magnetic resonance (ODMR)[4], commonly found in insulating materials like diamond and SiC, particularly advantageous[5,6]. At present, the field is dominated by diamond-based sensors utilizing nitrogen-vacancy (NV) centers, which have demonstrated exceptional performance across a range of sensing applications[7–9,10,11]. The development of NV centers embedded in fluorescence-collecting pillars on cantilevers has already progressed to a level, where they are commercially available[12,13]. However, strong magnetic fields misaligned with the NV center's symmetry axis induce sub-level mixing, which disrupts spin initialization via spin pumping[14]. This causes a loss of ODMR contrast, impairing the sensor's functionality in the presence of strong magnetic fields with arbitrary orientations. For instance, a 10 mT field at an angle of 10° causes a 60% reduction in sensitivity. The TR12 center, an intrinsic defect in diamond with a sharp zero-phonon-line (ZPL) at 471 nm, discovered in 1956[15], was shown in a prior study to exhibit high ODMR contrast even in the presence of strong arbitrarily oriented magnetic fields. This makes it a viable substitute for NV centers in sensing scenarios involving strong magnetic fields. However, when building on these prior findings, we found that the TR12 center lacks sufficient photostability, making it less favorable for single-defect applications. The TR12 center's ability to sense strong, arbitrarily oriented magnetic fields is primarily tied to its electronic level structure. With this in mind, we investigated the ST2 center - short for Stuttgart - as a potential replacement. Discovered in 2019 in Stuttgart, it shares the same electronic level structure as the TR12 center, along with a sharp ZPL at 446 nm, high ODMR contrast and a wide acceptance angle to strong magnetic fields. So far, no signs of photoinstability have been observed - even over timescales of several weeks under continuous excitation.

We conducted a comprehensive study on individual ST2 centers in diamond. A reliable method for creating ST2 centers is established. The resulting centers were characterized in terms of their optical and magnetic properties, revealing their electronic level structure. Additionally, we measured their sensing capabilities for magnetic and electric fields, as well as temperature, supported by a theoretical framework.

Results

Creation of ST2 centers

We initially discovered ST2 centers in a natural diamond of unknown origin and unclear treatment history by observing their sharp zero-phonon line in emission and reaction of their fluorescence to a magnetic field. The

[1]3rd Institute of Physics, University of Stuttgart, Stuttgart, Germany. [2]Helmholtz-Zentrum Dresden-Rossendorf, Institute of Ion Beam Physics and Materials Research, Dresden, Germany. [3]Institute for Quantum Optics, Albert-Einstein Allee 11, Ulm University, Ulm, Germany. [4]Institute for Materials Research, Hasselt University, Diepenbeek, Belgium. [5]College of Staten Island (CUNY), Staten Island, NY, USA. [6]Institute of Physics, University of Augsburg, Augsburg, Germany. [7]Centre for Integrated Quantum Science and Technology (IQST), Ulm, Germany. [8]Max Planck Institute for Solid State Research, Stuttgart, Germany.
✉e-mail: jonas.foglszinger@gmail.com

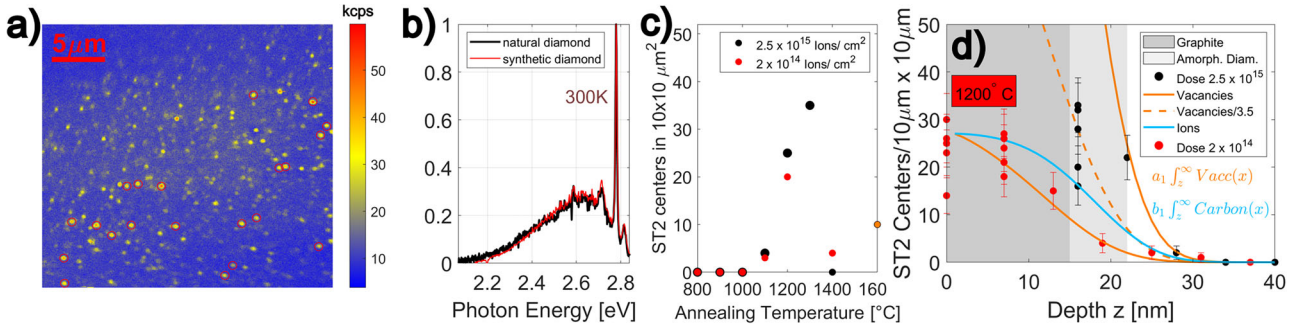

Fig. 1 | Identification and formation of ST2 centers in diamond. a Confocal scan image of the first synthetic diamond, covering a (27 μm × 27 μm) region. Several ST2 centers have been identified. Excitation was performed at 410 nm and fluorescence was collected from 450 to 525 nm. Other signatures observed in the scan, which were created by the same process, did not exhibit any particularly interesting features and were not investigated further. **b** Fluorescence spectra of two single ST2 centers—one in the natural diamond where the ST2 center was first discovered (black), and one in a synthetic diamond (red)—both recorded at room temperature under 410 nm excitation. **c** Dependence of the ST2 creation yield on the annealing temperature (1 h) for two different implantation doses, both at an implantation energy of 10 keV. **d** Depth profile of ST2 centers produced by one dose above and one below the graphitization threshold, followed by annealing at 1200 °C. The solid orange lines, derived from SRIM-TRIM simulations using the same proportionality constant a_1, fit both observed ST2 center distributions. The cyan profile of implanted carbon ions, derived from the same SRIM-TRIM simulations and displayed only for the lower dose, does not fit the observed data. At the dose above the graphitization threshold, an amorphous diamond layer was formed, inhibiting further ST2 center formation closer to the surface.

formation process of these centers was therefore unknown. Through systematic characterization of multiple synthetic diamond samples, we later discovered a method to reliably generate ST2 centers. The identified protocol was to implant the diamond with 10 keV ^{12}C ions at levels slightly above the graphitization threshold (2.5×10^{15} ions/cm^2), followed by annealing at 1200 °C for 1h (Methods section "Production" and Supplementary Notes 1 and 2). ST2 center creation was confirmed by locating individual centers in a confocal scan (Fig. 1a) and comparing their fluorescence spectrum to that of centers from the natural diamond (Fig. 1b) (more details in Methods section "Optical Characterization" and Supplementary Note 3). After the initial finding, we turned our attention to improving the efficiency of ST2 center production due to the low yield observed in the first attempts. In the following investigations, ST2 centers were never observed directly after implantation. They only emerged after sample annealing at 1100 °C or higher, as illustrated in Fig. 1c. When the annealing temperature exceeded 1300 °C, slight graphitization of the diamond's surface made it challenging to evaluate the formation efficiency, due to the partial destruction of the center-containing layer. Consequently, the observed reduction in yield at 1400 °C versus 1300 °C is derived from very limited data. At 1600 °C, a single sample with higher implantation energies, confirmed a noticeable drop in overall efficiency compared to 1200 °C and 1300 °C despite a significant increase in overall implantation damage also due to higher implantation energies. The highest yield was achieved after 1300 °C annealing with around 35 Centers in a 10 μm × 10 μm field. To gain deeper insights into the formation process of ST2 centers, the sample was etched in incremental steps, evaluating the remaining concentration of ST2 centers at each stage. The results, illustrated in Fig. 1d, revealed that the distribution of ST2 centers corresponds closely with the total vacancy profile resulting from implantation as simulated using SRIM-TRIM[16]. This suggests that the formation of ST2 centers is directly proportional to the implantation dose and independent of vacancy or interstitial migration. The exclusive use of carbon and the absence of foreign elements for the implantation, as described in Supplementary Note 1, suggest that these centers are intrinsic defects, comprising only interstitial sites and vacancies within the diamond lattice. This also fits the correlation between the concentration of ST2 centers and the vacancy profile. However, a significant challenge arises from the relatively low proportionality constant between the implantation dose and the resulting ST2 center concentration of about 2×10^{-8} centers/ion for 10 keV implantation energy. As the implantation dose increases, the sample starts to graphitize, forming amorphous diamond and non-diamond carbon phases where ST2 centers cannot form. This theoretically limits the maximum achievable yield of ST2 centers with this method, effectively capping the local density of these defects at an estimated threshold of around 6×10^4 centers per cubic micron or 120 centers in a 10 μm × 10 μm field for 10 keV implantation as pointed out in Supplementary Note 2. A first attempt to optimize the yield led to an increase from 30 to roughly 50 centers in 100 square microns, almost 50% of the theoretical maximum. Given these relatively low numbers, the current production method presents challenges for the scalability and practical deployment of ST2 centers in high-density sensing scenarios. Even applications that rely on single defects are impacted by this issue, due to the inherent statistical nature of the production process and the extensive lattice damage formed around the defect.

Optical properties of ST2 centers in zero magnetic field

Due to the low yield of ST2 centers, we observed them exclusively as single defects. A low-power antibunching measurement confirms their single-photon nature and reveals an excited state lifetime of 1.4 ns (Fig. 2b). The brightness of these defects, when optically saturated, was significantly affected by an external magnetic field, showing up to a twofold increase. The observed effect implies the presence of a sensitive spin state. Given that this effect occurs only during saturation, this spin state should be an excited state. Based on earlier observations in molecules[17], ST1[18,19] and TR12, the electronic level structure illustrated in Fig. 2a was suggested as the simplest explanation for the results observed thus far. This model, which includes a single ground state, an excited singlet state, and a metastable triplet, has consistently matched all subsequent data. We will therefore assume that this model is correct, while pointing out where our data serves as a consistency check. It is crucial to highlight that the fluorescence observed originates only from the transition between the singlet states. Consequently, the brightness of the centers is proportional to the total population in these singlets. For different lifetimes of the triplet sub-levels, CW ODMR causes a shift of population from longer-lived to shorter-lived states, which shows up as up to three separate ODMR lines in the spectrum. Experimental data from multiple single defects confirm this, with two transitions being detected at 495.3 MHz and 2267.5 MHz (Fig. 2c). The ODMR contrast also disappears when the laser-power is reduced, indicating that the triplet is an excited state which is only significantly populated under saturation conditions. The spin Hamiltonian of a triplet ($S = 1$) state at zero magnetic field is represented by $H = D(S_z^2 - S(S+1)/3) + E(S_x^2 - S_y^2)$. The parameters D = 1636.6 MHz and E = 896.6 MHz can be deduced from the measured ODMR resonance frequencies as confirmed in the next subsection. When microwave radiation is applied at both observed ODMR frequencies, the center displays coherent population trapping (CPT), as illustrated in Fig. 2d. This points to the existence of two long-lived states (Supplementary Note 4). It is clear from the width of the CPT resonance that these states have a lifetime of about

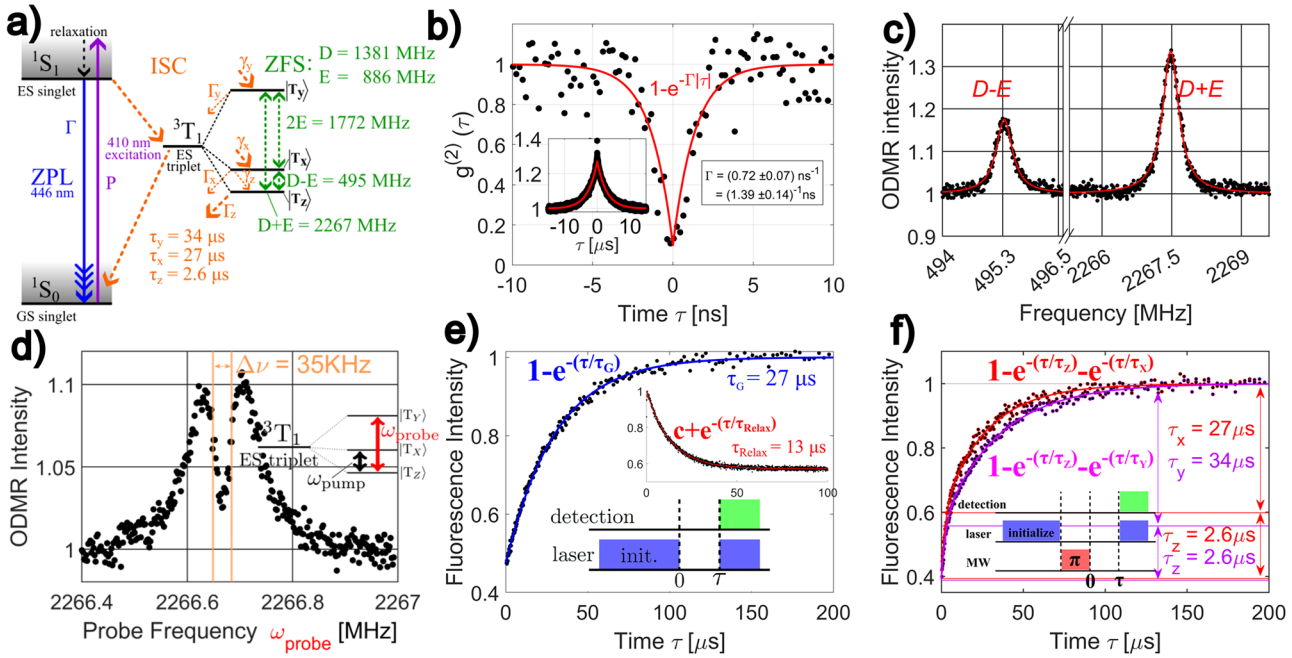

Fig. 2 | Optical detection of electron-spin dynamics in single ST2 defects. **a** Suggested level structure of the ST2 defect, featuring a singlet ground state, a singlet excited state, and an intermediate metastable triplet state accessible via intersystem crossing (ISC). **b** Low power anti-bunching measurement performed on a single ST2 center with a simple fit $1 - \exp -\Gamma|\tau|$, exhibiting a dip at $\tau = 0$ with a value below 0.5, indicating its single-photon nature. A more detailed analysis that accounts for the measurement devices' time jitter (350 ps) revealed no significant impact (see Supplementary Note 13). At optical saturation (inset), the measurement reveals a distinct bunching shoulder that does not appear at lower power levels, confirming the existence of the long lived triplet state $^3T_1$ shown in Fig. 2a, and revelas its rate of repopulation (details in Supplementary Note 13). **c** CW ODMR spectroscopy in zero magnetic field (ZFS), displaying two resonances. A third resonance could not be observed. **d** Coherent population trapping measurement revealing the presence of two long-lived states, T_x and T_y, with lifetimes of at least 10 µs. During this measurement one MW frequency ω_{pump} is fixed at the first ZFS resonance, while the other one, ω_{probe}, is swept across the second ZFS resonance. Further details are available in Supplementary Note 4. **e** Decay of the total metastable population, revealing only a single lifetime τ_G (blue line) consistent with the long-lived states T_x and T_y (Fig. 2f). The first inset illustrates the time-scale for fluorescence equilibration of the center after being initialized in the ground state by turning the laser off. The second inset displays the pulse sequence used to acquire the lifetime data. **f** Direct lifetime measurements for all triplet sublevels were performed by shifting the metastable population from one long-lived state into the short-lived T_z state using a π-pulse derived from Rabi oscillations. The inset displays the pulse sequence used to acquire both datasets.

10 µs or longer. The decay of the metastable population is directly observed by turning off the laser for a variable time τ. As the laser excitation is restored, there is a resulting temporary increase in fluorescence as the population in the singlets is increased, as depicted in Fig. 2e. The fit reveals only one decay time of roughly 27 µs. It is reasonable to assume that the short-lived sub-level T_z is minimally populated. Consequently, the lifetimes of the two long-lived states can be observed in isolation by applying a microwave π-pulse, derived from Rabi oscillations, to shift the population from the long-lived states T_x and T_y to the short-lived T_z (see Fig. 2f). The successful fitting of a double-exponential decay to this data, reveals all three lifetimes $\tau_x = 27$ µs, $\tau_y = 34$ µs and $\tau_z = 2.6$ µs. It confirms that the T_z state is the least populated state when the center is excited continuously. While the lifetime difference between T_x and T_y is minimal, it should lead to a weak ODMR signal when driving the transition between these states. Nonetheless, no ODMR signal has been observed at this frequency. The most reasonable explanation is that the effect is canceled due to the disparity in population strength between these states. Considering the transition rates into the metastable sub-levels T_i (γ_i), and out of these sub-levels (Γ_i) as illustrated in Fig. 2a, this requires the condition $\gamma_x/\Gamma_x = \gamma_y/\Gamma_y$ to be fulfilled (Supplementary Note 10). However, directly assessing the rates into the metastable triplet states γ_x, γ_y and γ_z is not straightforward. It can only be assessed indirectly through simulations that reproduce the ODMR contrast of the resonance lines. This comparison clearly contradicts the above relation and instead leads to $\gamma_x = \gamma_y$, which is required to match the difference in ODMR contrast observed in Fig. 2c (Supplementary Note 9).

The fluorescence intensity of the center at low excitation powers revealed the characteristics of a dipole transition when the linear polarization of the excitation laser is rotated (see Fig. 3b). Six distinct and recurring polarizations were observed for ST2 centers, one of which is shown in Fig. 3b. This finding offers an initial indication of the center's relatively low symmetry, which is further examined in the next subsection.

Fluorescence dependence on the magnetic field

The previously noted dependence of the ST2 center fluorescence arises because the applied magnetic field induces mixing of the excited triplet state sub-levels. Consequently, their lifetimes become intertwined, impacting the overall dynamics and brightness of the center. In this experiment, a permanent magnet ($10 \times 10 \times 10$ mm^3 NdFeB, magnetization 1.4 T perpendicular to the sample surface) is carefully positioned above the sample using stepper motors. As the magnet's position changes, the fluorescence intensity of the center is recorded, covering various magnetic field orientations (see Fig. 3a). This data provides the means to evaluate the center's sensitivity to strong external magnetic fields and gives insights into its symmetry and orientation. The dark spots in Fig. 3a result from the magnetic field being aligned with the principal axes of the triplet state, causing the corresponding sub-level to remain unaffected by the field. By measuring ODMR spectra for these specific orientations, we can validate the applicability of the theory for Spin 1 systems as described by $H = D(S_z^2 - S(S+1)/3) + E(S_x^2 - S_y^2) + g\mu_B \mathbf{S} \cdot \mathbf{B}$ to ST2 centers, incorporating the zero-field splitting parameters D and E, the Bohr magneton μ_B, electron g-factor $g = 2$ and $S = 1$. The ODMR frequencies for each magnetic field orientation can be derived from this Hamiltonian and its eigenstates. By comparing these frequencies with the observed ODMR data, we can accurately assign the sub-level orientations to the dark spots in the magnetic maps in Fig. 3a. Matching this with NV data reveals that the center's z-orientation corresponds to the [111] direction in diamond (Supplementary Note 7). Additionally, this allows for the

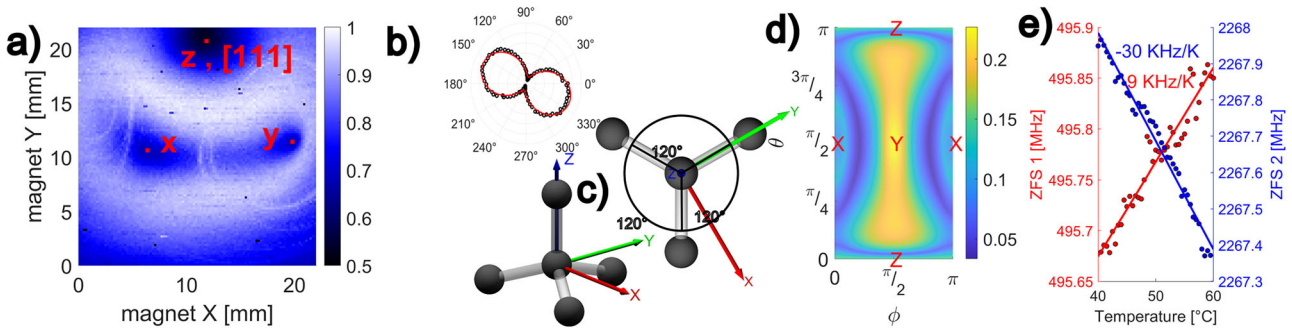

Fig. 3 | Magnetic field and temperature dependence of single ST2 centers in their metastable triplet state. a Fluorescence response of a single ST2 center based on magnet position. Points where the magnetic field aligns with a sub-level of the metastable triplet state are emphasized. These points are found by comparison with simulations described in Supplemenary Note 8. The faint rings arise due to cross relaxation mediated by nearby electron spins, explained in Supplementary Note 11. **b** Fluorescence dependence on the polarization of excitation light at low powers, revealing the characteristics of a dipole transition. Here one of the six dipole orientations is displayed. **c** Orientation of the principal axes of the metastable triplet state with respect to the diamond lattice, highlighting the threefold rotational symmetry inherent to the diamond lattice. **d** ODMR contrast simulation for ST2 as a function of magnetic field orientation at 30 mT. The figure shows the second highest ODMR contrast among the three available transitions which is the limiting factor for magnetic field sensitivity. The validity of this simulation is confirmed by the fact that it can reproduce the measured maps in Fig. 3a. These simulation results provide the best overall illustrations of the sensing capacity of ST2 centers for stronger magnetic fields. **e** Temperature dependence of the ZFS from 40 °C to 60 °C for a single ST2 center. The shifts for the resonance correspond to shifts of 10.5 kHz/K for D and −19.5 kHz/K for E. This suggests that ST2 centers can, in principle, also be used as temperature sensors.

assignment of zero-field transitions, which was assumed to be known in the preceding section. The g-factor $g = 2$ is validated by simulating the magnetic field strength at a particular distance from the magnet and comparing the findings to Fig. 3a. Additionally, simulating the rotation of the magnetic field based on the magnet's position helps to derive the exact x and y orientations in the laboratory frame. As illustrated in Fig. 3c, the *y*-axis of ST2 is situated in the plane formed by two adjacent σ-bonds. Also, the entire system can be simulated to analyze the overall dynamics and reproduce the measured magnetic maps. This simulation is primarily based on the level structure shown in Fig. 2a and is described in greater detail in the Supplementary Note 8. The simulated maps align perfectly with the measured data. As this simulation incorporates all measured transition rates and the level structure, it offers a reliable confirmation of the model. Based on these simulations, we also predict twelve species of differently oriented ST2 centers, organized into four triples. These correspond to four distinct σ-bond orientations and the threefold rotational symmetry of the diamond lattice along each of these bonds. Each orientation thereby gives its own characteristic magnetic map, most of which were confirmed in experiments (Supplementary Fig. 2). The twelve maps align with the six different directions of the optical dipole, with each direction comprising two magnetic orientations. The variety of orientations implies that the center must have a low symmetry group. With twelve different orientations, there are effectively only two symmetry candidates: inversion symmetry C_i and one mirror plane C_s. The lack of electric field sensitivity, which will be addressed later, indicates that the ST2 center exhibits inversion symmetry C_i.

ST2 as magnetic field sensors

The results in Fig. 3a, along with similar measurements (see Methods section "Characterization of Magnetic Properties"), provide insights into the effectiveness of ST2 as a magnetic field sensor. However, the intertwined nature of magnetic field strength and orientation due to the permanent magnet makes it difficult to isolate these variables, complicating the interpretation of said data. To make the situation more tangible, a simulation can be utilized in which magnetic field strength and orientation are separable. The same model used to reproduce the measured maps in Fig. 3a can also simulate the magnetic contrast of a single ST2 center. Further details on this simulation are provided in the supplementary Note 9. The result of such a simulation is shown in Fig. 3d. At a magnetic field strength of 30 mT, a significant ODMR contrast is available across nearly the entire 4π unit sphere. Given that the sensitivity is directly linked to the ODMR contrast of the center, this data confirms the suitability of ST2 centers as magnetic sensors, making them an excellent complement to NV centers. They enable the detection of strong magnetic fields in almost any orientation with high ODMR contrast, while maintaining the typically high spatial resolution associated with single defects. Exceptionally weak magnetic fields, where the induced frequency shift is comparable to or smaller than the zero-field splitting, are the only case where this does not apply. In such scenarios, the high E value converts the transitions into clock transitions, as the ODMR frequency shows no linear dependence on the magnetic field. This is particularly useful for temperature sensitivity and coherent population trapping (CPT) measurements, but it limits the magnetic sensitivity. However, this is precisely the regime where the NV center excels, as the opposite logic holds true for NV. Extremely weak magnetic fields do not cause significant state mixing, enabling the NV center to detect magnetic fields regardless of their orientation. Thus, this regime is already accounted for by the NV.

Given the low yield of ST2 centers, only single-defect uses are viable. The shot-noise limited magnetic sensitivity η for such a single ST2 center can be approximated by considering the shot-noise $\sigma = 10^2$ counts/$\sqrt{\text{Hz}}$, the maximum gradient of the ODMR spectrum $C_{\max} = 1$ count/kHz, and the frequency shift of ODMR resonances $C_M = 28$ GHz/T:

$$\eta = \frac{\sigma}{C_{max} C_M} = 3.6 \frac{\mu\text{T}}{\sqrt{\text{Hz}}} \tag{1}$$

The calculation is based on a conservative 5% ODMR contrast superimposed on a average 10 kcps fluorescence signal without any methods of fluorescence enhancement from a single ST2 center and a measured 0.65 MHz linewidth. The maximum gradient $C_{\max}$ equals the maximum derivative of a Lorentzian function with a full width at half maximum (FWHM) of 0.65 MHz and an amplitude of $A = 10^4 \cdot 0.05$ counts, which equals

$$C_{max} = \frac{A}{FWHM} \cdot \frac{3 * \sqrt{3}}{4} = 1 \text{ count/kHz}. \tag{2}$$

Overall, these results are very similar to those reported for TR12 and ST1[18,19]. That said, we found that ST2 centers tend to be more photostable, which makes them more promising for single-defect applications. Still, this qualitative impression needs to be confirmed through more detailed studies.

ST2 as a general sensing platform

To assess the broader capabilities of ST2 centers, we measured their sensitivity to electric fields and temperature.

To evaluate the electrical sensitivity of the ST2 center, we measured centers between two gold contacts connected to an external voltage source.

However, no shift in ODMR frequencies was detected even at electric field strengths as high as 2×10^6 V/m (see Supplementary Note 12). This observation aligns with the proposed inversion symmetry C_i for ST2 centers, which would preclude the existence of a permanent electric dipole and thus first order electrical sensitivity.

Using the PID-controlled aluminum holder described in the methods section D, ST2 ODMR frequencies were measured as a function of temperature between 40 °C and 60 °C. The temperature was stabilized for at least 5 min before each measurement. As shown in Fig. 3e, there is a clear linear dependence, with the two ODMR frequencies shifting by 9 kHz/K and −30 kHz/K, respectively. This shift is two to three times lower than that observed for NV centers with a shift of −74 kHz/K[3], suggesting that ST2 centers may not be preferable as primary temperature sensors in most applications. However, they in principle still show the potential to be used for local temperature assessment if convenient.

Discussion

ST2 centers can be produced in diamond using carbon implantation. However, the yield is quite low, with a conversion rate of approximately 2×10^{-8} centers per implanted ion at 10 keV implantation energy. This rate results in a maximum achievable density of ST2 centers of approximately 6×10^4 centers per cubic micron. Our findings reveal that the ST2 center features a sensitive spin state with coherent properties at room temperature. Through the combination of various measurements, we have outlined the full electronic level structure responsible for the dynamics of population within this spin state, as well as the overall properties of the center. By examining the dependence of fluorescence on excitation polarization and external magnetic field, we identified twelve inequivalent orientations of ST2 centers. Since no electric sensitivity was observed, we conclude that the ST2 center exhibits C_i symmetry. ST2 complements the existing NV sensing capabilities exceptionally well, as its strength aligns precisely where the NV center has limitations, and vice versa. ST2 is particularly effective for measuring strong magnetic fields of any orientation with high spatial resolution and can also be used for temperature measurements under ambient conditions. Fig. 3d, which displays a notable ODMR contrast for arbitrary orientations of a 30 mT magnetic field, provides the best illustration of this point. In comparison, if the angle between the NV symmetry axis and a 30 mT magnetic field is greater than 10°, its ODMR contrast decreases below 3%. Current efforts aim to transfer the NV center technology used in pillars on cantilevers to the ST2 center[12,13,20–22] (Me-Myself and I. Placeholder for Supplementary Info). Preliminary results from these initial efforts are encouraging. Such sensors could be used to study the internal structure of nano-scale magnetic textures, such as skyrmions, with randomly aligned magnetic field orientations. The main challenge is the exceptionally low yield of ST2 centers using the current production method, which prevents the process from being economically scalable. Addressing this issue is therefore the highest priority. Furthermore, resolving this problem may facilitate progress toward achieving electroluminescence and electrical readout for ST2 centers.

Methods

Production

ST2 centers (Fig. 1a, b) were produced by implanting ^{12}C ions at energies between 5 keV and 500 keV into the (100) plane of CVD diamond, followed by annealing at temperatures between 800 °C and 1600 °C. The depth profile of these shallow-implanted centers was determined by incrementally etching the diamond surface using reactive ion etching (RIE) with O_2-plasma, while monitoring the concentration of remaining centers (Fig. 1d). Using optical lithography and electron beam physical vapor deposition (EBPVD), Au-contacts were deposited on the sample, facilitating the application of microwaves and DC voltages. The diodes were subsequently connected to external measurement systems via wire bonding.

Optical characterization

The defects in the prepared sample were analyzed using a home-built confocal microscope with 410 nm linearly polarized laser excitation (Supplementary Fig. 1). This excitation source was used for all optical experiments presented in this study. Fluorescence emitted from the sample was directed to a single-photon detector, and a confocal scan was generated by moving the excitation point via a 3D piezo-stage. The detection window was set from 450 nm to 525 nm. This detection window was used consistently across all optical experiments presented in this study. The excitation and detection points were kept coincident at all times. In such confocal scans, the first step was to identify ST2 centers. For this purpose, the fluorescence light was redirected to a spectrometer to record the optical spectrum, as shown in Fig. 1b. The sharp zero-phonon line (ZPL) at 446 nm served as the primary identification feature in these spectra. The final step in verification involved measuring the ODMR spectrum, which confirmed the defect through the presence of two prominent resonance lines at 495.3 MHz and 2267.5 MHz.

Characterization of magnetic properties

To probe the magnetically susceptible spin states of the center, microwaves were applied to the sample through one of the integrated gold contacts. Given that the spin states are excited states, as shown in the electronic level structure of ST2 (Fig. 2a), it was critical to use a powerful laser to optically saturate the center for these measurements. A permanent magnet was precisely moved into proximity of the sample using stepper motors, creating a magnetic field at the sample's position. This arrangement enabled the exploration of the centers' sensing capabilities in the presence of strong arbitrarily oriented magnetic fields.

Thermal sensitivity

For a thorough evaluation of temperature sensitivity, the sample was mounted on a solid aluminum holder with an integrated PID-controlled heater. The cool environment of the lab, combined with this set-up, ensured precise temperature control with a precision of less than 0.1 K. The aluminum holder thereby served as a thermal mass to stabilize the temperature.

Data availability

The data sets used to generate the figures in this manuscript are publicly available at [https://doi.org/10.5281/zenodo.15839755]. Additional data supporting the conclusions of this study are available from the corresponding author upon reasonable request.

Code availability

The MATLAB simulation code that supports the findings of this work is available from the corresponding author upon reasonable request.

Received: 31 December 2024; Accepted: 18 September 2025;
Published online: 16 March 2026

References

1. Rembold, P. et al. Introduction to quantum optimal control for quantum sensing with nitrogen-vacancy centers in diamond. *AVS Quantum Science* **2**, 024701 (2020).
2. Rovny, J. et al. New opportunities in condensed matter physics for nanoscale quantum sensors. Preprint at https://doi.org/10.48550/arXiv.2403.13710 (2024).
3. Liu, C.-F. et al. Ultra-sensitive hybrid diamond nanothermometer. *Nat. Sci. Rev.* **8**, nwaa194 (2021).
4. Brossel, J. & Bitter, F. A new "double resonance" method for investigating atomic energy levels. application to Hg^3p_1. *Phys. Rev.* **86**, 308–316 (1952).
5. Staudacher, T. et al. Nuclear magnetic resonance spectroscopy on a (5-nanometer)3 sample volume. *Science* **339**, 561–563 (2013).
6. Zaitsev, A. *Optical Properties of Diamond* (Springer, 2001).
7. Acosta, V. M. et al. Dynamic stabilization of the optical resonances of single nitrogen-vacancy centers in diamond. *Phys. Rev. Lett.* **108**, 206401 (2012).
8. Fuchs, G. D. et al. Excited-state spin coherence of a single nitrogen–vacancy centre in diamond. *Nat. Phys.* **6**, 668–672 (2010).

9. Shen, Y., Sweeney, T. M. & Wang, H. Zero-phonon linewidth of single nitrogen vacancy centers in diamond nanocrystals. *Phys. Rev. B* **77**, 033201 (2008).
10. Dolde, F. et al. Electric-field sensing using single diamond spins. *Nat. Phys.* **7**, 459–463 (2011).
11. Kucsko, G. et al. Nanometre-scale thermometry in a living cell. *Nature* **500**, 54–58 (2013).
12. Ren, Y. & Takahashi, S. Detection of electron paramagnetic resonance of two electron spins using a single nv center in diamond. *APL Quantum* **1**, 046108 (2024).
13. Qnami. Quantum sensing leaders in nanoscale precision. https://qnami.ch/wp-content/uploads/2021/03/Quantum-Foundry-Case-Study-16.03.2021.pdf.
14. Tetienne, J.-P. et al. Magnetic-field-dependent photodynamics of single nv defects in diamond: an application to qualitative all-optical magnetic imaging. *New J. Phys* **14**, 103033 (2012).
15. Clark, C. D., Ditchburn, R. & Dyer, H. The absorption spectra of natural and irradiated diamonds. *Proc. R. Soc. Lond. Ser. A, Math. Phys. Sci.* **234**, 363–381 (1956).
16. Ziegler, J. F., Ziegler, M. D. & Biersack, J. P. Srim – the stopping and range of ions in matter (2010). *Nuclear Instruments Methods Phys. Res. Section B: Beam Interact. Mater. Atoms* **268**, 1818–1823 (2010).
17. Wrachtrup, J., von Borczyskowski, C., Bernard, J., Orrit, M. & Brown, R. Optically detected spin coherence of single molecules. *Phys. Rev. Lett.* **71**, 3565–3568 (1993).
18. Balasubramanian, P. et al. Discovery of st1 centers in natural diamond. *Nanophotonics* **8**, 1993–2002 (2019).
19. Lee, S.-Y. et al. Readout and control of a single nuclear spin with a metastable electron spin ancilla. *Nat. Nanotechnol.* **8**, 487–492 (2013).
20. Momenzadeh, S. A. et al. Nanoengineered diamond waveguide as a robust bright platform for nanomagnetometry using shallow nitrogen vacancy centers. *Nano Lett.* **15**, 165–169 (2015).
21. Me-Myself and I. Placeholder for supplementary info.
22. Morigi, G., Eschner, J. & Keitel, C. H. Ground state laser cooling using electromagnetically induced transparency. *Phys. Rev. Lett.* **85**, 4458–4461 (2000).

Acknowledgements

We thank Michelle Schweitzer for proofreading the manuscript. This work was supported by Bundesministerium für Bildung und Forschung (project UNIQ), Deutsche Forschungsgemeinschaft (grant KO4999/3-1), FET-Flagship Project SQUARE, EU project AMADEUS, DFG research group FOR 2724 and QTBW. Support from the Ion Beam Center (IBC) at HZDR is acknowledged for ion implantation.

Author contributions

The majority of the experiments were conducted by J.F. with contribution from R.K. The optimization and characterization of the samples were performed by J.F., L.K., A.D., and P.S. The implantation was performed by G.V.A., M.S., L.K., and A.D. The sample annealing was carried out by A.M.Z., A.D., and J.Fu. The data analysis and simulation were performed by J.F. with contributions from all authors. J.F. wrote the manuscript from feedback from all authors. R.K., P.S., F.J., and J.W. supervised the work.

Funding

Open Access funding enabled and organized by Projekt DEAL.

Competing interests

The authors declare no competing interests.

Additional information

Supplementary information The online version contains supplementary material available at https://doi.org/10.1038/s41534-025-01116-8.

Correspondence and requests for materials should be addressed to Jonas Foglszinger.